Extreme Mechanics Letters 45 (2021) 101271

Contents lists available at ScienceDirect

Extreme Mechanics Letters

journal homepage: www.elsevier.com/locate/eml

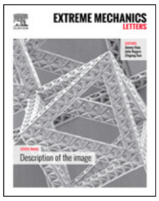

Orientation and stress state dependent plasticity and damage initiation behavior of stainless steel 304L manufactured by laser powder bed fusion additive manufacturing

Shipin Qin [a], Zhuqing Wang [a], Allison M. Beese [a,b,*]

[a] *Department of Materials Science and Engineering, The Pennsylvania State University, University Park, PA 16802, USA*
[b] *Department of Mechanical Engineering, The Pennsylvania State University, University Park, PA 16802, USA*

ARTICLE INFO

Article history:
Received 9 October 2020
Received in revised form 16 January 2021
Accepted 21 January 2021
Available online 11 March 2021

Keywords:
Powder bed fusion
Stainless steel 304L
Multiaxial plasticity model
Multiaxial fracture

ABSTRACT

The plasticity and ductile fracture behavior of stainless steel 304L fabricated by laser powder bed fusion additive manufacturing was investigated under both uniaxial and multiaxial loading conditions through the use of specialized geometry mechanical test specimens. Material anisotropy was probed through the extraction of samples in two orthogonal material directions. The experimentally measured plasticity behavior was found to be anisotropic and stress state dependent. An anisotropic Hill48 plasticity model, calibrated using experimental data, was able to accurately capture this behavior. A combined experimental–computational approach was used to quantify the ductile fracture behavior, considering both damage initiation and final fracture. An anisotropic Hosford–Coulomb model was used to capture the anisotropic and stress state dependent fracture behavior.

1. Introduction

Laser powder bed fusion (L-PBF) additive manufacturing (AM) of metals involves a repetitive process of spreading of a thin layer of powder over a baseplate, using a laser heat source to melt the powder in the 2D pattern of the current layer, and cooling and solidification of the current layer to make 3D components [1]. Compared to traditional manufacturing techniques, AM methods enable rapid prototyping, increased design flexibility, and part customization [2].

Austenitic stainless steel 304L (SS304L) has been processed through AM methods, and it has been shown to maintain its high strength, ductility, and corrosion resistance compared to its wrought counterparts [3,4]. However, most existing studies on additively manufactured SS304L have focused on its mechanical behavior under uniaxial loading conditions [3–6]. The behavior of additively manufactured materials under realistic multiaxial loading conditions must be understood for the reliable adoption of AM for load-bearing complex-shaped components.

The multiaxial plasticity behavior of SS304L manufactured by directed energy deposition (DED) AM has been characterized [7,8]. The authors investigated the plasticity behavior of the material under five different loading conditions, and adopted a stress state dependent model to capture the strain hardening behavior. Other materials made by AM whose multiaxial plasticity behavior have been investigated include L-PBF Ti-6Al-4V [9,10], DED Ti-6Al-4V [11,12], and L-PBF SS316L [13]. However, the multiaxial deformation and failure behavior of L-PBF SS304L, an important alloy for industries including nuclear and chemical [14–16], has not been reported.

In this study, the multiaxial plasticity and fracture behavior of L-PBF SS304L were characterized through a combined experimental and computational approach. The multiaxial deformation behavior was probed using specimens with a uniform gauge section, resulting in spatially homogeneous strain fields, and fracture tests were performed on specimens with a nonuniform gauge section, resulting in heterogeneous strain fields. An anisotropic plasticity model was developed and implemented into finite element simulations. The proposed plasticity model was validated using data from experiments with both uniform and nonuniform gauge regions. Additionally, an anisotropic damage initiation model is proposed, which captures the stress state- and direction-dependent damage initiation behavior of L-PBF SS304L observed through the fracture experiments.

2. Experiments

2.1. Materials

L-PBF AM (3DSystems ProX DMP 320) was used to fabricate SS304L walls using pre-alloyed SS304L powder with the elemental composition given in Table 1. The powder used was gas

---

* Corresponding author at: Department of Materials Science and Engineering, The Pennsylvania State University, University Park, PA 16802, USA.
E-mail address: amb961@psu.edu (A.M. Beese).

https://doi.org/10.1016/j.eml.2021.101271

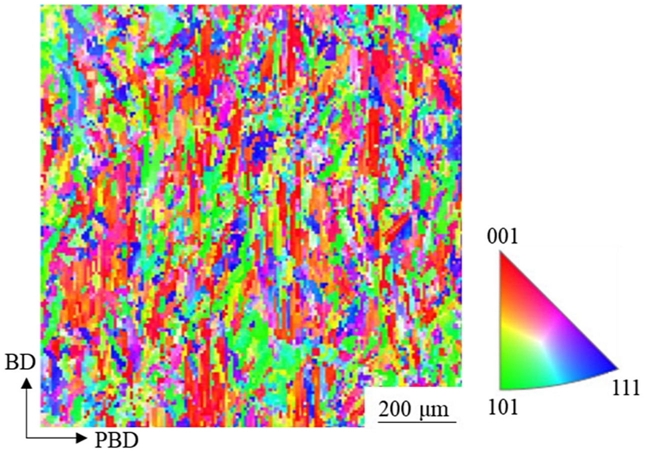

Fig. 1. EBSD map of the cross-section from a uniaxial tension sample, with the colors representing the *hkl* plane normals along the thickness direction (out of the page). BD indicates build direction, and PBD indicates perpendicular build direction. (For interpretation of the references to color in this figure legend, the reader is referred to the web version of this article.)

atomized in nitrogen (Carpenter Powder Products, Corp.), with a diameter range between 15 μm and 45 μm. A laser power of 300 W, scanning speed of 900 mm/s, hatch spacing of 0.1 mm, and layer thickness of 60 μm were used for fabrication. Before removing the walls from the baseplate, the entire build was subjected to a stress relief at 650° for 3 h in an argon atmosphere (Solar Atmospheres).

To characterize the microstructure, a sample from the SS304L wall was mounted in epoxy, ground, and polished using standard metallographic techniques with a final polish using a 0.05 μm colloidal silica suspension. The polished sample was then observed using electron backscatter diffraction (EBSD; Oxford Nordlys Max2), which revealed that the grains were randomly oriented but elongated along the build direction, as shown in Fig. 1. The elemental composition of the walls was analyzed through combustion infrared detection for C, through inert gas fusion for N, and through direct current plasma emission spectroscopy for other elements (Luvak Inc., Boylson, MA) as shown in Table 1. The measured C and N content conforms to the ASTM standard E1019-11 and all other measured elemental concentrations conform to ASTM standard E1097-12.

2.2. Plasticity tests

2.2.1. Uniaxial tension

Uniaxial tension specimens, with gauge sections measuring 21.5 mm × 4 mm × 1.5 mm (see Fig. 2a), in accordance with ASTM E8, were extracted from the SS304L walls along both the build direction (BD) and the perpendicular build direction (PBD) by wire electrical discharge machining (EDM). An electromechanical testing frame equipped with a 10 kN load cell (Instron 4202) was used to perform uniaxial tension tests at a strain rate of 1.2×10^{-3} s^{-1}. The strain fields were determined using digital image correlation (DIC). For DIC analysis, the gauge region of each sample was painted with a white background followed by a black random speckle pattern. A digital camera (Point Grey GRAS-50S5M-C) was set up to take images, at 1 Hz, of the gauge region during deformation. Correlation software (Vic2D, Correlated Solutions) was used to analyze the evolution of the deformation fields in the recorded images using a cubic B-spline interpolation algorithm. A subset size of 21 pixels and a step size of 5 pixels were used in the analysis, equivalent to a virtual strain gauge length of 56 pixels or 1.5 mm. The strain along the vertical direction was computed using a 21 mm long virtual extensometer.

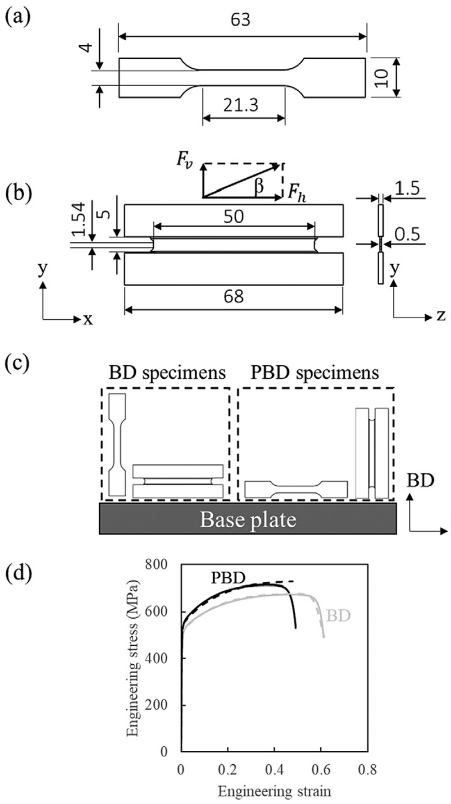

Fig. 2. Geometries of the (a) uniaxial tension and (b) multiaxial plasticity specimens [17], with the angle β, which describes the ratio of applied vertical force, F_v, to horizontal force, F_h, denoted. All dimensions are in mm. (c) Schematic of sample orientation with respect to build orientation. (d) Engineering stress versus strain curves under uniaxial tension along two directions obtained from experiments (solid lines) and finite element simulations (dashed lines)

2.2.2. Multiaxial loading

Multiaxial plasticity specimens along both the BD and the PBD were extracted from the SS304L walls by EDM as shown in Fig. 2b and c. The large width-to-length ratio and small thickness in the gauge region result in plane strain along the horizontal (x) direction and plane stress through the thickness (z) direction.

A custom-built dual-actuator hydraulic test frame (MTS Systems Corp.) was used to perform multiaxial loading tests. The vertical force, F_v, was measured using two 100 kN load cells and the horizontal force, F_h, was measured using a 50 kN load cell. The ratio of vertical to horizontal applied load in various tests can be described by the angle, β, expressed as:

$$\tan\beta = \frac{F_v}{F_h} \tag{1}$$

such that $\beta = 0°$ results in pure shear, $\beta = 90°$ results in plane strain tension, and $0° < \beta < 90°$ results in combined tension and shear. In this work, $\beta = 0°$, 30°, 60°, and 90° were studied with the loading rates shown in Table 2.

The surface deformation fields of plasticity specimens were analyzed using DIC with a subset size of 25 pixels and a step size of 6 pixels, equivalent to a virtual strain gauge size of 67 pixels or 0.8 mm. The strains along the vertical and horizontal directions were computed using 3 mm long virtual extensometers along the two directions. For more details about this technique, refer to Ref. [17].

Table 1
Elemental composition (wt.%) of the pre-alloyed SS304L powder and a L-PBF SS304L wall.

	C	N	Si	Mn	Cr	Ni	Mo
SS304L powder	0.018	0.06	0.6	1.4	18.4	9.8	0.01
SS304L wall	0.020 ± 0.005	0.053 ± 0.005	0.62 ± 0.01	1.40 ± 0.03	18.22 ± 0.36	9.57 ± 0.19	0.006 ± 0.001

Table 2
Stress or strain loading rates applied in mechanical tests.

	Vertical loading rate	Horizontal loading rate
Plane strain tension	3.3×10^{-4} /s	0 /s
Pure shear	0 /s	1.3×10^{-4} /s
Combined loading with $\beta = 30°$	2.1 MPa/s	3.6 MPa/s
Combined loading with $\beta = 60°$	3.6 MPa/s	2.1 MPa/s

2.3. Fracture tests

Fracture tests were performed on central hole specimens and notched tension specimens, whose geometries are shown in Fig. 3a, extracted from the SS304L walls by EDM. The central hole specimen has a through-thickness hole with a radius of 1.6 mm at the specimen center, to provide a state of nearly constant uniaxial tension to failure at the vertical surface of the hole. The notched tension specimens have two round notches on the sides of the gauge section to provide data for failure under stress states between uniaxial tension and plane strain tension. In the current study, specimens with three different notch radii were manufactured: 2.67 mm, 4 mm, and 8 mm. All fracture tests were performed along both BD and PBD.

All of the fracture specimens were tested on an electromechanical loading frame equipped with a 10 kN load cell (MTS Criterion Model 43) at a loading rate of 0.01 mm/s. The strain fields on the specimen surface were analyzed by DIC using a subset of 29 pixels and a step size of 7 pixels, corresponding to a virtual strain gauge size of 78 pixels or 2 mm. The displacement was measured using a virtual extensometer at the specimen center, the length of which was 12 mm for the central hole specimens and 15 mm for the notched tension specimens.

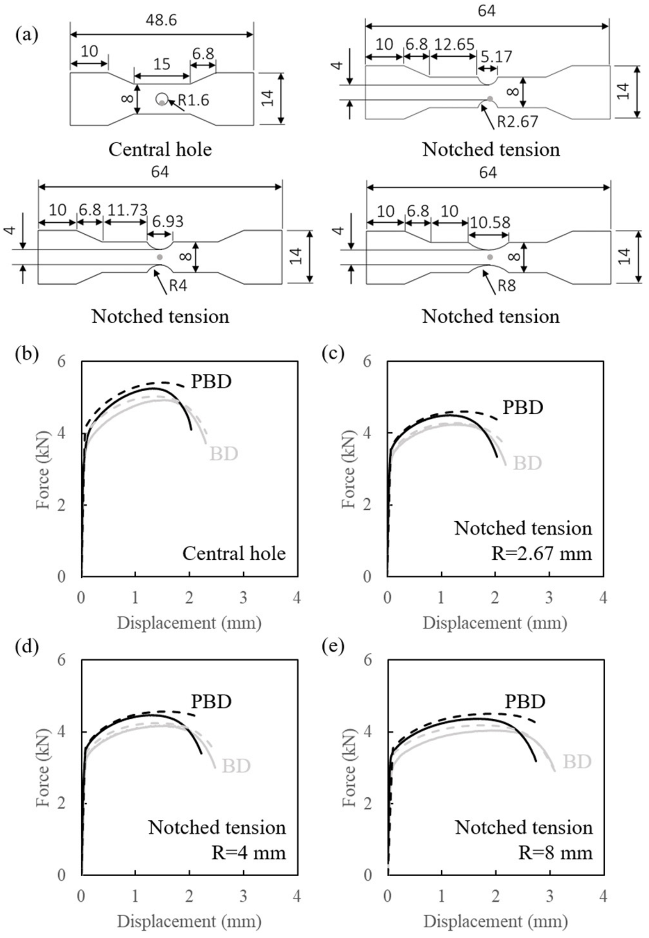

Fig. 3. (a) Geometries of central hole and notched tension specimens (all dimensions in mm). The gray points (at the mid-point through the thickness) indicate where fracture is expected to initiate in each geometry. (b-e) Force versus displacement curves for central hole (b) and notched tension with R = 2.67 mm (c), R = 4 mm (d), and R = 8 mm (e), showing comparisons between experiment (solid lines) and finite element simulations (dashed lines)

3. Plasticity model

As the thickness of the specimens in the present study was 1.5 mm or less, the through thickness stress is negligible, and therefore, the plasticity model will be presented for plane stress. In what follows, the Cauchy stress vector $\boldsymbol{\sigma}$ will be denoted as

$$\boldsymbol{\sigma} = [\sigma_{11}, \sigma_{22}, \sigma_{12}]^T \tag{2}$$

with 1 denoting the material direction parallel to the PBD, and 2 denoting the material direction parallel to the BD. Similarly, the plastic strain vector $\boldsymbol{\varepsilon}^p$ will be denoted as

$$\boldsymbol{\varepsilon}^p = \left[\varepsilon^p_{11}, \varepsilon^p_{22}, \varepsilon^p_{12}\right]^T \tag{3}$$

When the material is subjected to a load, plastic yielding can be assumed to take place when the following criterion is met:

$$\Phi\left(\boldsymbol{\sigma}\right) = \overline{\sigma}_{Hill48} - \sigma_y = 0 \tag{4}$$

where $\Phi\left(\boldsymbol{\sigma}\right)$ is the yield potential, and

$$\overline{\sigma}_{Hill48} = \sqrt{(\boldsymbol{P} \cdot \boldsymbol{\sigma}) \cdot \boldsymbol{\sigma}}, \text{ with}$$

$$\boldsymbol{P} = \begin{bmatrix} P_{11} & P_{12} & 0 \\ P_{12} & 1 & 0 \\ 0 & 0 & P_{33} \end{bmatrix} \tag{5}$$

is the Hill48 equivalent stress [19]. The yield stress, σ_y, is a scalar function of the equivalent plastic strain $\overline{\varepsilon}^p$. In the current study, this scalar function is taken to be:

$$\begin{aligned} &\dot{\sigma}_y = nA\left(\varepsilon_0 + \dot{\overline{\varepsilon}}^p\right)^{n-1} \text{ for } \overline{\varepsilon}^p \le \overline{\varepsilon}^p_{necking} \\ &\dot{\sigma}_y = K\dot{\overline{\varepsilon}}^p \text{ for } \overline{\varepsilon}^p > \overline{\varepsilon}^p_{necking} \end{aligned} \tag{6}$$

where A, ε_0, and n are the Swift law parameters [12], K is the slope of linear extrapolation after necking, and $\overline{\varepsilon}^p_{necking}$ is the strain level when necking starts in uniaxial tension.

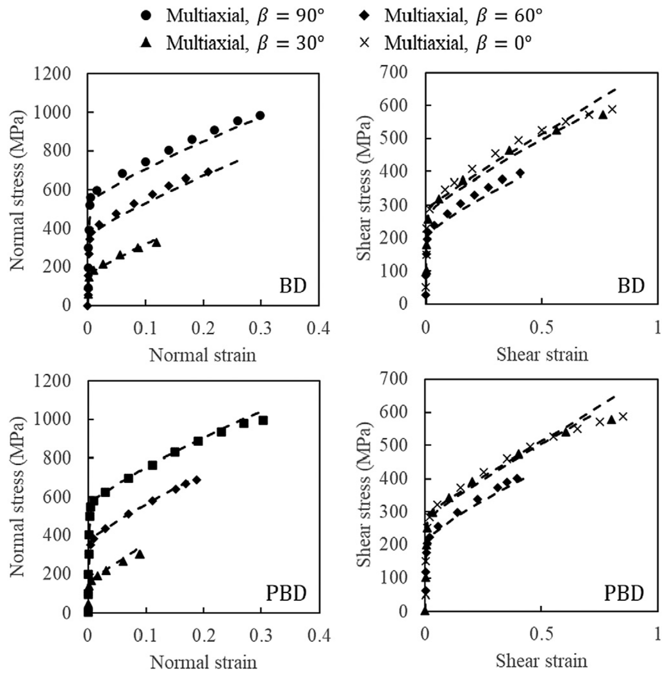

Fig. 4. Normal and shear true stress versus strain curves for multiaxial loading conditions from experiments (symbols) and simulations (lines)

The associated flow rule, which determines the increment of the plastic strain tensor, is assumed and is defined as:

$$\dot{\boldsymbol{\varepsilon}}^p = \dot{\gamma}\frac{\partial\Phi(\boldsymbol{\sigma})}{\partial\boldsymbol{\sigma}} \tag{7}$$

where $\dot{\gamma}$ is the plastic multiplier.

The work conjugate equivalent plastic strain $\bar{\varepsilon}^p$ can be calculated incrementally through:

$$d\bar{\varepsilon}^p = \sqrt{\frac{\left(d\varepsilon_{11}^p\right)^2 + P_{11}\left(d\varepsilon_{22}^p\right)^2 - 2P_{12}d\varepsilon_{11}^p d\varepsilon_{22}^p + \frac{1}{P_{33}}\left(2d\varepsilon_{12}^p\right)^2}{P_{11} - P_{12}^2}} \tag{8}$$

4. Results and discussion

4.1. Calibration of the model parameters

The plasticity model above requires the calibration of the following parameters: P_{11}, P_{12}, P_{33}, A, ε_0, n, and K. P_{11}, P_{12}, and P_{33} describe the orientation and stress state dependence of the plasticity behavior; therefore, in the current study, they were determined by comparing the following test results along both the BD and PBD: the stress–strain curves in uniaxial tension, the normal stress–strain curves in plane strain tension ($\beta = 90°$), and the shear stress–strain curves in pure shear loading ($\beta = 0°$). The Swift law parameters, A, ε_0, and n, were determined by fitting the strain hardening curve obtained from uniaxial tension along the BD. In this test, $\bar{\varepsilon}^p_{necking} = 0.37$.

As the strain hardening behavior beyond necking cannot be determined experimentally, the slope of the linear extrapolation K was determined iteratively through finite element analysis (FEA). Specifically, the uniaxial tension test along BD was simulated using the finite element software ABAQUS [20]. One eighth of the specimen was modeled, and symmetric boundary conditions were applied along all three cut planes. The geometry was discretized with 8320 hexahedron elements, with the smallest element being located at the center and having a size of 0.1 mm. A uniform upward displacement was applied to the top of the model, and the simulated engineering stress–strain curve was compared to that in experiments. In the iterative approach, the slope K was adjusted so that the simulated engineering stress–strain curves agree with experimental data, as shown in Fig. 2d. All calibrated parameters are given in Table 3.

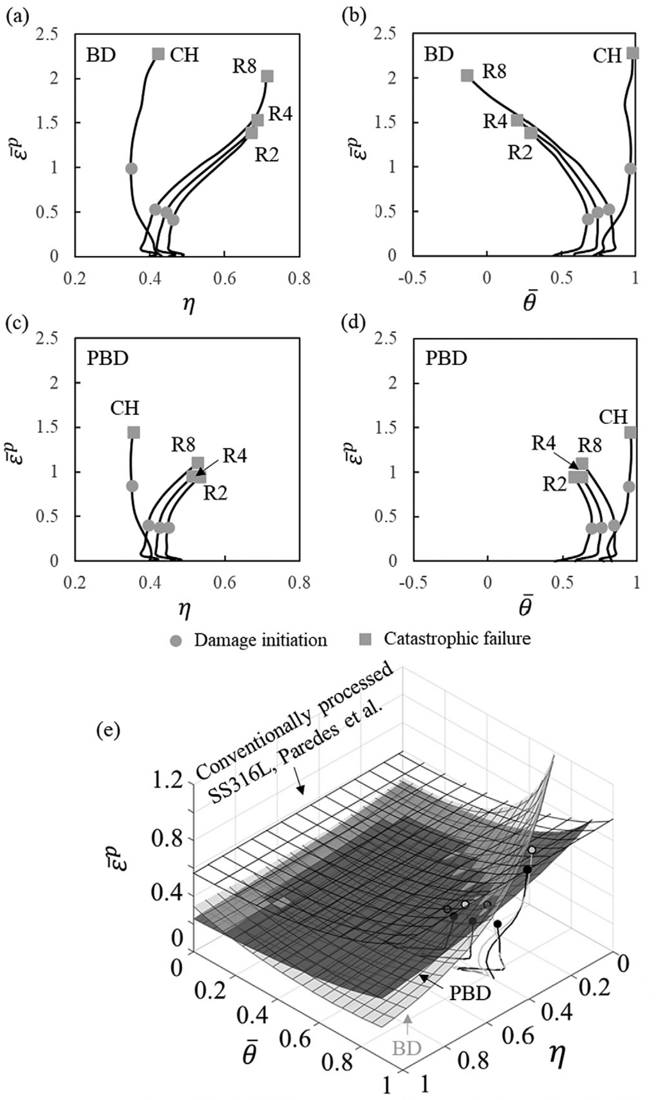

Fig. 5. (a–d) Evolution of stress triaxiality ($\boldsymbol{\eta}$) and Lode angle parameter ($\bar{\boldsymbol{\theta}}$) at the damage initiation sites marked in Fig. 3a of the central hole and notched tension specimens along (a, b) the build direction (BD) and (c, d) perpendicular build direction (PBD), where results from central hole (CH) and notched tension (R R2, R4, and R8) specimens are presented. Damage initiation is taken to be at the displacement to maximum force observed in experiments, and catastrophic failure corresponds to experimentally observed total sample fracture. (e) Damage initiation surface representing the calibrated anisotropic Hosford–Coulomb failure model along the BD and PBD. The lines show the 3D path of plastic strain versus stress triaxiality and Lode angle parameter up to damage initiation (symbols). Due to the evolution of stress state during experiments, the symbols should not be expected to lie on the surfaces. A fracture surface for conventionally processed SS316L, as reported by Paredes et al., is presented for comparison [18].

4.2. Plasticity model validation

The calibrated plasticity model was validated through finite element simulations of the uniaxial tension test along the PBD, the multiaxial loading tests along both directions, and the notched

Table 3
Calibrated Hill48 and anisotropic Hosford–Coulomb (HC) model parameters for L-PBF SS304L.

Hill48	P_{11}	P_{12}	P_{33}	A	ε_0	n	K
	0.90	−0.30	3.17	1386 MPa	0.167	0.551	1043 MPa
HC	a	b	c	d	M_{12}	M_{22}	M_{44}
	0.623	1.671	0.096	0.193	0.107	1.404	0.976

Table 4
Hill48 equivalent plastic strain values at the moments of damage initiation and catastrophic failure. BD indicates build direction, and PBD indicates perpendicular build direction.

	Damage initiation		Catastrophic failure	
	BD	PBD	BD	PBD
Notched tension R = 2.67 mm	0.42	0.38	1.39	0.95
Notched tension R = 4 mm	0.50	0.38	1.53	0.95
Notched tension R = 8 mm	0.53	0.40	2.03	1.10
Central hole	0.99	0.84	2.28	1.45

tension and central hole tension tests along both directions. For uniaxial tension, the finite element model introduced in Section 4.1 was adopted but the loading direction in the simulation was altered to PBD. The comparison in Fig. 2d shows that the model captured the anisotropic strain hardening behavior under uniaxial tension. The stress–strain behavior right before fracture, which was not captured by the simulation, can be explained by the difference in damage accumulation rate resulting from the initial microstructure in which grains were elongated along the BD (e.g., Ref. [21]).

The simulations of multiaxial loading experiments were performed using a single element model with a cubic element (ABAQUS element type C3D8 [20]). In all of the simulations, the bottom of the element was fixed. For plane strain tension ($\beta = 90°$) and pure shear loading ($\beta = 0°$), a uniform displacement was applied to the top surface, and for combined loading ($\beta = 60°$ or $30°$), a vertical and a horizontal force was applied to the top surface, with their ratio being consistent with the corresponding β value intended to be simulated. The simulated normal and shear stress–strain curves are compared to experimental results in Fig. 4, and good agreement was achieved.

Comparison of experimentally observed and computationally simulated force–displacement behavior for fracture specimens also serves as a partial validation of the plasticity model. For each of the fracture test specimens, one eighth of the geometry was modeled in ABAQUS [20], and symmetry boundary conditions were applied along all three cut planes. All of the geometries were discretized by hexahedron elements (element type C3D8 [20]), with the element size decreasing towards the center of the specimen. A mesh size study revealed that when the element size at the center was 0.05 mm or smaller, the local $\bar{\varepsilon}^p$ value at the center at final failure increased by no more than 1.8% when the element size was decreased by half for all of the geometries. Therefore, a minimum mesh size of 0.05 mm was adopted, which resulted in 3101 elements for the central hole specimen, and for notched tension specimens, 2597 elements for R = 2.67 mm, 2611 elements for R = 4 mm, and 2457 elements for R = 8 mm. The simulated force–displacement curves were compared to their respective experimental results in Fig. 3b–e. In general, good agreement was achieved, but the simulations overestimated the force levels in the central hole and R = 8 mm notched tension tests.

4.3. Stress state dependent fracture behavior

Fracture tests were performed on central hole specimens and notched tension specimens, as introduced in Section 2.3. These specimens have a nonuniform gauge section at their center, so that the deformation concentrates at the specimen vertical center upon deforming, and damage initiates from the edge of the hole for the central hole specimen and from the center point of the specimen for the notched tension specimens, as marked in Fig. 3a. Different geometries or notch radius results in different stress state at the point of damage initiation. Stress state can be described by two variables, stress triaxiality, η, and Lode angle parameter, $\bar{\theta}$, defined as:

$$\eta = \frac{\sigma_m}{\bar{\sigma}_{vM}}$$

$$\bar{\theta} = 1 - \frac{2}{\pi} \arccos\left(\frac{3\sqrt{3}}{2}\frac{J_3}{\sqrt{J_2^3}}\right) \tag{9}$$

where $\sigma_m = (\sigma_{11} + \sigma_{22} + \sigma_{33})/3$ is the hydrostatic stress, $\bar{\sigma}_{vM} = \sqrt{3J_2}$ is the von Mises stress, and $J_2 = \frac{1}{2}s_{ij} : s_{ij}$ and $J_3 = \det\left(s_{ij}\right)$ are the second and third invariants of the deviatoric stress tensor s_{ij}, respectively. It has been shown in the literature that the evolution of both stress triaxiality and Lode angle parameter is important in describing the stress state dependence of ductile fracture in metals [22,23].

As the fracture test specimens have a nonuniform gauge section, and damage initiates at the through-thickness midplane, the strain and stress at the point of damage initiation cannot be measured experimentally. Therefore, the simulation results presented in Section 4.2 were adopted for extracting the evolution of strain and stress state during deformation. Fig. 5a-d show the evolution of the Hill48 equivalent plastic strain, η, and $\bar{\theta}$ at the damage initiation sites. Also shown in the figure are the moment of damage initiation for each condition, defined as the moment of maximum force in experiments, and catastrophic failure, defined as the moment before full sample separation. A comparison of the strain levels at damage initiation and catastrophic fracture is shown in Table 4. On average, the strain levels at damage initiation along the BD were 23% higher than those along the PBD. The strain levels at catastrophic failure exhibited a more significant orientation dependence, with those along the BD being 62% higher than those along the PBD. It can also be observed from Fig. 5a–d that the material was more damage-tolerant along the BD than along the PBD, as demonstrated by the significantly higher strain range spanning damage initiation to catastrophic failure along the BD. This orientation dependence is likely due to the initial sample anisotropy with grains elongated along the BD. The evolution of stress state during loading, as evidenced by the change of η and $\bar{\theta}$ with increasing strain in all of the tests, highlights the importance of considering loading history for an accurate description of ductile failure.

To describe the anisotropy of the damage initiation behavior, the anisotropic Hosford–Coulomb model is adopted, which has been shown to be able to capture the anisotropic fracture behavior of both conventionally processed metals [24] and additively manufactured metals [13]. In the anisotropic Hosford–Coulomb model, a damage indicator D is calculated as:

$$D = \int_0^{\bar{\varepsilon}} \frac{1}{\bar{\varepsilon}_{HC}} d\bar{\varepsilon}^p, \ \text{with}$$

$$\bar{\varepsilon}_{HC} = b\left(\frac{1+c}{g_{HC}\left(\frac{\boldsymbol{M}\tilde{\boldsymbol{\sigma}}}{\bar{\sigma}}\right)}\right)^{\frac{1}{d}} \tag{10}$$

where b, c, and d are model parameters, $\overline{\varepsilon}^p$ is the Hill48 equivalent plastic strain defined in Eq. (8), and $\boldsymbol{M}$ is a transformation matrix defined as:

$$\boldsymbol{M} = \begin{bmatrix} 1 & M_{12} & 0 & 0 & 0 & 0 \\ 0 & M_{22} & 0 & 0 & 0 & 0 \\ 0 & 0 & 1 & 0 & 0 & 0 \\ 0 & 0 & 0 & M_{44} & 0 & 0 \\ 0 & 0 & 0 & 0 & 1 & 0 \\ 0 & 0 & 0 & 0 & 0 & 1 \end{bmatrix} \tag{11}$$

and g_{HC} is a function of the Cauchy stress vector $\tilde{\boldsymbol{\sigma}} = [\sigma_{11}, \sigma_{22}, \sigma_{33}, \sigma_{12}, \sigma_{23}, \sigma_{31}]^T$:

$$g_{HC}\left(\frac{\boldsymbol{\sigma}}{\overline{\sigma}}\right) = \left\{\frac{1}{2}\left[(f_1 - f_2)^a + (f_2 - f_3)^a + (f_1 - f_3)^a\right]\right\}^{\frac{1}{a}} + c\,(2\eta + f_1 + f_3) \tag{12}$$

where a is a model parameter, and f_1, f_2, and f_3 are defined as:

$$\begin{aligned} f_1 &= \frac{2}{3}\cos\left[\frac{\pi}{6}\left(1 - \overline{\theta}\right)\right] \\ f_2 &= \frac{2}{3}\cos\left[\frac{\pi}{6}\left(3 + \overline{\theta}\right)\right] \\ f_3 &= -\frac{2}{3}\cos\left[\frac{\pi}{6}\left(1 + \overline{\theta}\right)\right] \end{aligned} \tag{13}$$

The model was calibrated using data from the fracture tests and simulations along both orientations in the current study, resulting in the parameters in Table 3. In the calibration, all variables ($\overline{\varepsilon}^p$, η, and $\overline{\theta}$) were extracted from simulations, with the integration in Eq. (10) performed up to the moment of maximum force in experiments. The calibrated damage initiation surface for proportional loading is schematically shown in Fig. 5e. Comparison of the surfaces shows that damage would initiate in specimens along BD first only when subjected to loads whose η and $\overline{\theta}$ values are both relatively high. In other stress states, damage would initiate first in specimens along PBD. The surface also shows that the damage initiation behavior of L-PBF SS304L exhibits a stronger stress state dependence along the BD than along the PBD. Note that the surfaces can only be regarded as the exact fracture initiation strain for proportional loading. The above model is phenomenological, meaning that defects like pre-existing pores (e.g., lack of fusion or gas entrapment pores) or voids produced during material damage, are not explicitly included, but rather, the model predicts damage initiation of the material through a metric defined in a continuum sense.

In Ref. [18], Paredes et al. investigated the stress state dependent fracture behavior of a conventionally processed stainless steel (SS316L), and calibrated the modified Mohr–Coulomb (MMC) model to describe this behavior. This fracture surface is also included in Fig. 5e. Compared to the additively manufactured SS304L in the current study, the fracture behavior of conventionally processed SS316L, as presented by Parades et al. [18], exhibited less stress state dependence, as indicated by the flatness of its fracture surface. The increased stress state dependence, and anisotropy, of the fracture behavior of additively manufactured SS304L may be attributed to small lack of fusion defects, gas porosity, and elongated grains. Note that from Fig. 5e, one cannot conclude that the conventionally processed SS316L is more ductile than the additively manufactured SS304L because the definition of fracture is different — in the current study, the failure locus was defined in terms of the moment of maximum force, while in Ref. [18], the failure locus was defined in terms of force dropping rate (i.e., somewhere between maximum force and final material separation).

5. Summary

In this study, the multiaxial plasticity and stress state dependent fracture behavior of L-PBF SS304L along two different orientations was investigated through experiments and modeling, both of which are critical for an accurate description and prediction of mechanical behavior of materials under load. The key findings of this study include:

- The yield and strain hardening behavior of L-PBF SS304L was found to be anisotropic and stress state dependent. An anisotropic Hill48 plasticity model was able to capture both behaviors accurately.
- Within the stress state range studied, the strain level at damage initiation ($\eta > 0.33$ and $\overline{\theta} > 0.64$) and catastrophic failure ($\eta > 0.33$ and $\overline{\theta} > -0.14$) of L-PBF SS304L was found to be higher along build direction than along perpendicular build direction, and the damage accumulation rate along the build direction was significantly slower than that along the perpendicular build direction.
- The calibrated anisotropic Hosford–Coulomb model showed that the damage initiation behavior of L-PBF SS304L had stronger stress state dependence along the build direction than along the perpendicular build direction.

Declaration of competing interest

The authors declare that they have no known competing financial interests or personal relationships that could have appeared to influence the work reported in this paper.

Acknowledgments

The authors gratefully acknowledge the financial support provided by the National Science Foundation, USA through award numbers CMMI-1402978 and CMMI-1652575.

References

[1] T. DebRoy, H.L. Wei, J.S. Zuback, T. Mukherjee, J.W. Elmer, J.O. Milewski, A.M. Beese, A. Wilson-Heid, A. De, W. Zhang, Additive manufacturing of metallic components – Process, structure and properties, Prog. Mater. Sci. 92 (2018) 112–224.

[2] T.D. Ngo, A. Kashani, G. Imbalzano, K.T.Q. Nguyen, D. Hui, Additive manufacturing (3D printing): A review of materials, methods, applications and challenges, Composites B: Engineering 143 (2018) 172–196.

[3] K. Guan, Z. Wang, M. Gao, X. Li, X. Zeng, Effects of processing parameters on tensile properties of selective laser melted 304 stainless steel, Mater. Des. 50 (2013) 581–586.

[4] Z. Wang, T.A. Palmer, A.M. Beese, Effect of processing parameters on microstructure and tensile properties of austenitic stainless steel 304L made by directed energy deposition additive manufacturing, Acta Mater. 110 (2016) 226–235.

[5] T. Pan, S. Karnati, Y. Zhang, X. Zhang, C.H. Hung, L. Li, F. Liou, Experiment characterization and formulation estimation of tensile properties for selective laser melting manufactured 304L stainless steel, Mater. Sci. Eng. A 798 (2020) 140086.

[6] H. Yu, J. Yang, J. Yin, Z. Wang, X. Zeng, Comparison on mechanical anisotropies of selective laser melted Ti-6Al-4V alloy and 304 stainless steel, Mater. Sci. Eng. A 695 (2017) 92–100.

[7] Z. Wang, A.M. Beese, Stress state-dependent mechanics of additively manufactured 304L stainless steel: Part 1 – characterization and modeling of the effect of stress state and texture on microstructural evolution, Mater. Sci. Eng. A 743 (2019) 811–823.

[8] Z. Wang, A.M. Beese, Stress state-dependent mechanics of additively manufactured 304L stainless steel: Part 2 – Characterization and modeling of macroscopic plasticity behavior, Mater. Sci. Eng. A 743 (2019) 824–831.

[9] A.E. Wilson-Heid, S. Qin, A.M. Beese, Anisotropic multiaxial plasticity model for laser powder bed fusion additively manufactured Ti-6Al-4V, Mater. Sci. Eng. A 738 (2018) 90–97.

[10] A.E. Wilson-Heid, A.M. Beese, Fracture of laser powder bed fusion additively manufactured Ti–6Al–4v under multiaxial loading: Calibration and comparison of fracture models, Mater. Sci. Eng. A (2019) 137967.

[11] M.B. Gorji, T. Tancogne-Dejean, D. Mohr, Heterogeneous random medium plasticity and fracture model of additively-manufactured Ti-6Al-4V, Acta Mater. 148 (2018) 442–455.
[12] T. Tancogne-Dejean, C.C. Roth, U. Woy, D. Mohr, Probabilistic fracture of Ti-6Al-4V made through additive layer manufacturing, Int. J. Plast. 78 (2016) 145–172.
[13] A.E. Wilson-Heid, S. Qin, A.M. Beese, Multiaxial plasticity and fracture behavior of stainless steel 316L by laser powder bed fusion: Experiments and computational modeling, Acta Mater. 199 (2020) 578–592.
[14] D.E. Nivens, P.D. Nichols, J.M. Henson, G.G. Geesey, D.C. White, Reversible acceleration of the corrosion of aisi 304 stainless steel exposed to seawater induced by growth and secretions of the marine bacterium vibrio natriegens, Corrosion 42 (4) (1986) 204–210.
[15] S.J. Zinkle, G.S. Was, Materials challenges in nuclear energy, Acta Mater. 61 (3) (2013) 735–758.
[16] J.D. Heald, E. Kiss, Low cycle fatigue of nuclear pipe components, J. Pressure Vessel Technol. 96 (3) (1974) 171–176.
[17] D. Mohr, M. Oswald, A new experimental technique for the multi-axial testing of advanced high strength steel sheets, Exp. Mech. 48 (1) (2008) 65–77.
[18] M. Paredes, V. Grolleau, T. Wierzbicki, On ductile fracture of 316L stainless steels at room and cryogenic temperature level: An engineering approach to determine material parameters, Materialia (10) (2020) 100624.
[19] R. Hill, A theory of the yielding and plastic flow of anisotropic metals, Proc. R. Soc. A Math. Phys. Eng. Sci. 193 (1033) (1948) 281–297.
[20] Abaqus user manual v2017, DS SIMULIA, 2017.
[21] A.E. Wilson-Heid, Z. Wang, B. McCornac, A.M. Beese, Quantitative relationship between anisotropic strain to failure and grain morphology in additively manufactured Ti-6Al-4V, Mater. Sci. Eng. A 706 (2017) 287–294.
[22] Y. Bai, T. Wierzbicki, Application of extended Mohr–Coulomb criterion to ductile fracture, Int. J. Fract. 161 (1) (2010) 1–20.
[23] M. Luo, M. Dunand, D. Mohr, Experiments and modeling of anisotropic aluminum extrusions under multi-axial loading – Part II: Ductile fracture, Int. J. Plast. 32–33 (2012) 36–58.
[24] G. Gu, D. Mohr, Anisotropic Hosford–Coulomb fracture initiation model: Theory and application, Eng. Fract. Mech. 147 (2015) 480–497.